

Alma Mater Studiorum Università di Bologna
Archivio istituzionale della ricerca

Metabolic fingerprinting strategy: investigation of markers for the detection of extra virgin olive oil adulteration with soft-deodorized olive oils

This is the final peer-reviewed author's accepted manuscript (postprint) of the following publication:

Published Version:

Navratilova K., Hurkova K., Hrbek V., Uttl L., Tomaniova M., Valli E., et al. (2022). Metabolic fingerprinting strategy: investigation of markers for the detection of extra virgin olive oil adulteration with soft-deodorized olive oils. FOOD CONTROL, 134(April 2022), 1-8 [10.1016/j.foodcont.2021.108649].

Availability:

This version is available at: <https://hdl.handle.net/11585/856290> since: 2022-02-11

Published:

DOI: <http://doi.org/10.1016/j.foodcont.2021.108649>

Terms of use:

Some rights reserved. The terms and conditions for the reuse of this version of the manuscript are specified in the publishing policy. For all terms of use and more information see the publisher's website.

This item was downloaded from IRIS Università di Bologna (<https://cris.unibo.it/>).
When citing, please refer to the published version.

(Article begins on next page)

1
2
3
4
5
6
7
8
9
10
11
12
13
14
15
16
17
18
19
20
21
22
23
24
25
26
27
28
29
30
31
32

This is the final peer-reviewed accepted manuscript of:

Audrey Waldvogel, Andrea Fasolini, Francesco Basile, Sébastien Thomas, and Anne-Cécile Roger, Effect of the Support Synthetic Method on the Activity of Ni/CeZrPr Mixed Oxide in the Co-Methanation of CO₂/CO Mixtures for Application in Power-to-Gas with Co-Electrolysis, Energy & Fuels 2021 35 (16), 13304-13314

The final published version is available online at:

<https://doi.org/10.1021/acs.energyfuels.1c01524>

Terms of use:

Some rights reserved. The terms and conditions for the reuse of this version of the manuscript are specified in the publishing policy. For all terms of use and more information see the publisher's website.

1
2
3 1 Effect of the support synthetic method on the activity of Ni/CeZrPr mixed oxide in the co-methanation of
4 2 CO₂/CO mixtures for application in Power-to-Gas with co-electrolysis

6 3 Audrey Waldvogel¹, Andrea Fasolini^{1,2}, Francesco Basile², Sébastien Thomas¹ and Anne-Cécile Roger^{1*}
7
8 4 ¹ Institut de Chimie et Procédés pour l'Energie, l'Environnement et la Santé (ICPEES, UMR CNRS 7515), 25 rue
9 5 Becquerel, 67087 Strasbourg, France

11 6 ²Dipartimento di Chimica Industriale “Toso Montanari”, Alma Mater Studiorum - Università di Bologna, Viale
12 7 del Risorgimento 4, 40136 Bologna, Italy

8 Abstract

9 Synthetic Natural Gas (SNG) is an efficient option for transforming renewable energy into carbon neutral
16 fuels, while using a plug-and-play infrastructure, supporting the transition to renewable energy, paving the
17 way for a hydrogen-based economy. Captured CO₂ can be processed with water through high temperature
18 co-electrolysis, where reduction to CO and H₂ production by water splitting occurs. The outlet gas, composed
19 of CO₂, CO, H₂ and small amounts of CH₄, can be used to produce SNG by methanation of CO and CO₂ with
20 hydrogen. Among the parameters influencing the methanation reactions, the characteristics of the support
21 and its interaction with the metallic active phase, usually Ni, are of crucial importance and can be tuned by
22 the synthesis of the support. For this reason, three different synthetic methods, namely, pseudo sol-gel,
23 coprecipitation and colloidal combustion, were applied to the synthesis of a Ce/Zr/Pr oxide. The supports
24 were fully characterized by nitrogen physisorption, XRD, SEM-EDS, TPR and H₂-TPD before and after
25 impregnation with 10 wt%. Ni. The coprecipitated catalyst provided the best performances when submitted
26 to CO₂/CO co-methanation and typical post co-electrolysis mixture thanks to a combination of different
27 characteristics such as high surface area and mesoporosity, which allowed good Ni dispersion and surface
28 area, high support metal interaction and reducibility. Finally, the effect of Pr seemed to be beneficial,
29 increasing the methane yield at low temperatures.
30
31

33 24 Keywords

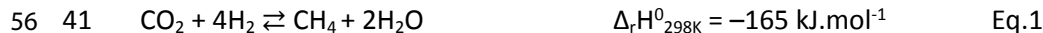
34
35 25 Ni/CeZrPr oxide, CO_x methanation, pseudo sol-gel, colloidal combustion, coprecipitation.

1. Introduction

Chemical storage of decarbonized electricity associated with chemical recycling of CO₂ has been identified as a key aspect needed for the energy transition our society has to face [1–4]. Although H₂ has been recognized as a suitable energy carrier, its implementation is still slowed down by technological, infrastructural and cultural aspects [5–7]. Transition to a hydrogen-based economy cannot be immediate and requires time to build the appropriate infrastructure. Nevertheless, the existing and well-developed methane network is available for Synthetic Natural Gas (SNG) to be fed, thus leading to a ready-to-use renewable feedstock. This technology Power-To-SNG contributes to mitigating CO₂ emissions, allowing greater penetration of intermittent renewable sources of electricity production.

48 35 This work is part of a project that aims to produce methane from water and captured CO₂, converted into a
49 36 CO/H₂ mixture by high-temperature co-electrolysis. In this system, CO₂ is fed into a water electrolyser where
50 37 CO, H₂ and even a small amount of CH₄ are produced. The resulting outlet gas consists of a mixture of CO,
51 38 CO₂ and H₂ [8,9]. In addition, residual steam and methane fractions may be present. The objective of this
52 39 study is to synthesize an active catalyst capable of producing methane from this mixture.

54 40 The process of methane production from CO, CO₂ and H₂ is governed by the following exothermic reactions:





The Sabatier reaction (Eq.1), also known as CO₂ methanation, has been widely studied, with Ni being the most investigated active phase due to its relatively cheap price, high selectivity for methane and good activity [10,11]. The characteristics and composition of the support also influence the methanation activity [10–13]. Ce-Zr based supports have been widely investigated in catalysis due to their good redox properties given by Ce which is increased by the presence of Zr into the oxide structure [14–17]. The addition of small fractions of Pr has been reported to increase the number of oxygen vacancies [15,18–21] leading to relatively high oxygen storage capacity (OCS) and may positively affect the activity of the. In addition, the presence of Pr and Zr increases the thermal stability of the support [14,15]. A range of Ce/Zr oxides has been applied as catalytic supports in the methanation reaction [10,22–25]. The addition of Zr to Ce enhanced the rate of methane production by having a positive effect on Ni dispersion [22]. An active and stable methanation catalyst was also obtained by Siakavelas *et al.* by doping CeO₂ with Pr₂O₃ [26]. The incorporation of Pr into the ceria lattice increases basicity and oxygen vacancies, with a positive effect on activity while reducing sintering. However, the application of ternary CeZrPr oxides has not been yet reported for the methanation reaction.

As the preparation method is expected to have a strong effect on the properties of ceria-based mixed oxides [27], such as BET surface, OCS and oxygen vacancies, in this study, three supports with the same Ce_{0.33}Zr_{0.63}Pr_{0.04}O_{1.99} composition were synthesized by three different techniques to investigate the effect of the preparation method on the properties of the supports as well as of the final catalysts. Pseudo sol-gel, coprecipitation in carbonate form and colloidal combustion methods were selected for this work. The first two methods are commonly used for the preparation of mixed oxide catalysts, whereas the third method is reported to favour the mesoporosity and enhanced BET surface [28]. The three methodologies allow obtaining materials with different textural properties that may affect the catalytic activity. For example, Frey *et al.* [25] reported that high surface area mesoporous materials with high Ni dispersion contribute to increasing the activity and stability of the catalysts. However, the work from Aldana *et al.* [29] regarding Ni on CeZr oxide, showed that carbon dioxide hydrogenation occurs between CO₂ adsorbed on the support and hydrogen chemisorbed on Ni. Catalytic sites at the interface between Ni and Ce-based support are thus important to favour the reaction, and the presence of a metal-support interaction may contribute to reaction enhancement [30]. Methanation of CO occurs, conversely, by CO dissociation on Ni, which competes with dissociative chemisorption of hydrogen, particularly at high H₂/CO ratios [31]. Here three synthetic methodologies, i.e., pseudo sol-gel, coprecipitation and colloidal combustion syntheses, were chosen to tailor the morphological properties of CeZrPr supports and their interplay with the Ni active phase in terms of dispersion and metal-support interaction.

The synthesized materials were fully characterized and tested under CO/CO₂ methanation conditions and post co-electrolysis conditions, to evaluate how the textural properties of the synthesized oxides influence metal-support interaction, Ni dispersion and catalytic activity. Finally, the best performing Ni/CeZrPr catalyst was compared with an analogous Ni/CeZr one (Ni/Ce_{0.34}Zr_{0.66}O_{2.00}), to evidence the role of the presence of Pr in the support structure.

2. Experimental

2.1. Catalyst synthesis

The support synthesis methodologies widely affect the overall catalytic properties [25,32–35]. In this study, the Ce_{0.33}Zr_{0.63}Pr_{0.04}O_{1.99} support was synthesized employing three different routes: pseudo sol-gel (CZP-SG), coprecipitation (CZP-CP) and colloidal combustion (CZP-CC). A schematic representation of the main steps of the three modes of preparation is given in Figure 1. The preparation pathways are detailed hereafter for 4.0 g of support.

* corresponding author : annececile.roger@unistra.fr

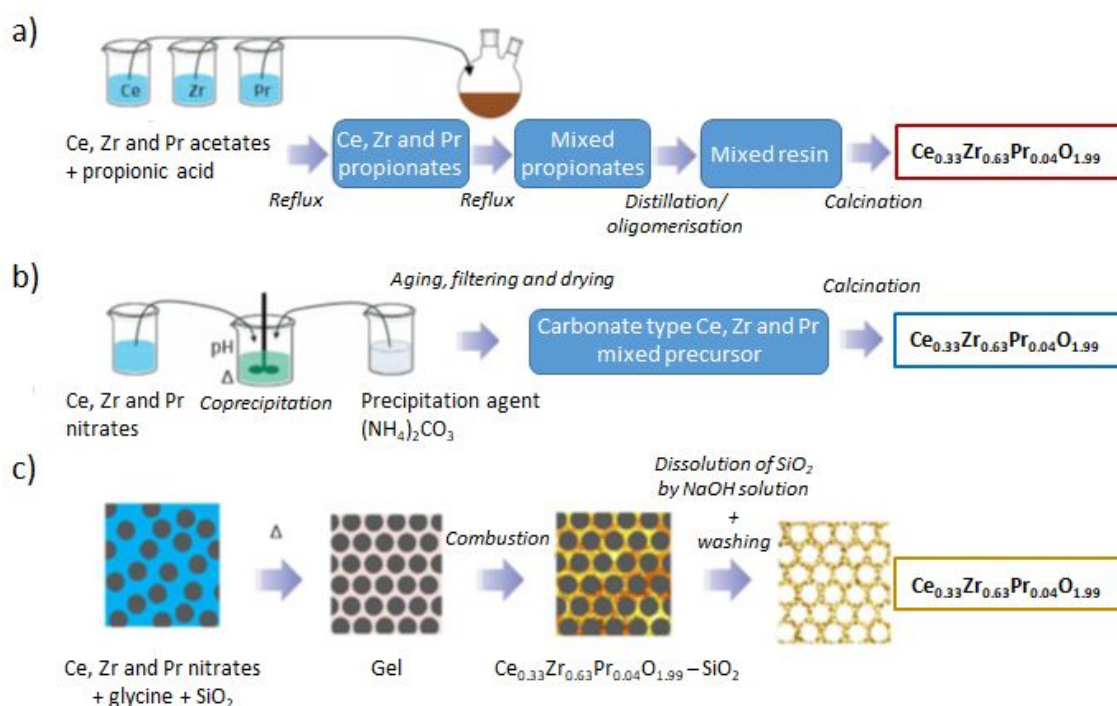


Figure 1: Schematic representation of the synthesis of CZP oxides by: (a) pseudo sol-gel, (b) coprecipitation and (c) colloidal combustion.

The sol-gel method is based on the formation of Ce, Zr, Pr propionates and their thermal decomposition. Differently from classic sol-gel synthesis, the propionates precursors form oligomers without leading to colloidal particles. In the synthesis 3.22 g of cerium acetate hexahydrated (99.9%, Alfa Aesar), 8.70 g of zirconium acetylacetonate (98% Strem Chemicals) and 0.42 g of praseodymium acetate (98% Strem Chemicals) were separately dissolved in hot propionic acid for 60 min to obtain 0.12 M_{cations} solutions. The three solutions were mixed and refluxed for 90 min at 141 °C, giving formation to mixed propionates by oligomerization. The solvent was then removed by distillation under vacuum. This led to a propionate gel, which was solidified using liquid nitrogen and then calcined under air at 500 °C for 6 h with a ramp of 2.0 °C min^{-1} .

Coprecipitation leads to the formation of a solid by simultaneous precipitation of the Ce^{3+} , Zr^{4+} et Pr^{3+} cations. A mass of 4.06 g of cerium nitrate hexahydrate (99.5% ACROS Organics), 6.05 g of zirconium oxynitrate hexahydrate (99% Sigma-Aldrich) and 0.49 g of praseodymium nitrate hexahydrate (99.9%, Sigma-Aldrich) were dissolved in water to reach a 0.20 M_{cations} solution. Another solution was prepared by dissolving ammonium carbonate in water (1,60 M). A beaker whose bottom was filled with water was kept at 65°C and pH 6.5. Then the cation and carbonates solution were simultaneously added dropwise to the beaker, keeping the pH constant during the addition. A 3.5 h aging was then performed and the obtained solid was filtered and washed with distilled water. The solid was dried at 100 °C for 1 h and then calcined under air at 500 °C for 6 h with a ramp of 2.0°C min^{-1} . The $\text{Ce}_{0.34}\text{Zr}_{0.66}\text{O}_{2.00}$ oxide was synthesised with the same procedure, removing praseodymium nitrate from the precursors' solution.

The colloidal combustion technique is based on the work of Voskanyan *et al.* [28] and consists of the addition of a fuel (glycine), a comburant (precursors of Ce, Zr and Pr) and colloidal SiO_2 particles. Combustion then removes the organic compounds while silica is removed by alkaline wash. A mass of 4.06 g of cerium nitrate hexahydrate (99.5% ACROS Organics), 6.05 g of zirconium oxynitrate hexahydrate (99% Sigma-Aldrich) and 0.49 g of praseodymium nitrate hexahydrate (99.9%, Sigma-Aldrich) were dissolved in 30 mL of water together with 2.4 g of glycine. Then 6 mL of SiO_2 colloidal solution (LUDOX TMA colloidal SiO_2 , 34 wt% of a

suspension in water of SiO₂ with a dimension of 20-22 nm, $\rho = 1.23 \text{ g mL}^{-1}$, Sigma-Aldrich) were added to the solution. The mixture was heated up to 160 °C in an oil bath to produce combustion. After cooling, the obtained powder was poured into a solution of NaOH 2.0 M at 80 °C and kept for 4 h. Washing with distilled water and ethanol gave the final support precursor which was dried at 100 °C and then calcined under air at 500 °C for 6 h with a ramp of 2.0 °C min⁻¹.

Ni impregnation was carried out by dissolving 2.2 g of nickel nitrate hexahydrate (98.5%, Sigma-Aldrich) in water and stirring this solution together with the support powders (4.0 g) for 15 min. After drying at 100 °C for 2 h, the impregnated powders were calcined at 500 °C for 6 h with a ramp of 2 °C min⁻¹. The final loading of the impregnated catalysts was 10.0 wt%Ni/support.

2.2. Catalyst characterization

The specific surface area and porous volume were measured, using a Micromeritics ASAP 2420 apparatus, by nitrogen adsorption-desorption at -196 °C. The specific surface area were calculated through Brunauer-Emmet-Teller (BET) method whereas porous volumes were estimated from the value at $P/P^\circ = 0.99$. A pretreatment at 250 °C under vacuum was performed on the samples to remove moisture and possible adsorbed species.

In order to study the phase composition of the obtained supports, X-ray diffraction analyses were carried out on a Bruker D8 Advance diffractometer equipped with a copper source and a LynxEye detector. The analyses were performed in a 2θ range between 10.0 and 100.0° at a scan rate of 0.059° 2θ and acquisition of 2.0 s per step.

SEM/EDS analyses were performed with a JEOL FEG 6700F Instrument equipped with an EDS analysis system.

The redox properties of the bare supports and impregnated catalysts were investigated employing temperature programmed reduction (TPR) on a Micromeritics AutoChem II 2920 apparatus. In a typical experiment around 150 mg of sample were submitted to a 50 NmL min⁻¹ flow of a 10% H₂/Ar mixture and heated up to 900 °C at 15 °C min⁻¹, then kept at this temperature for 30 min.

Metallic nickel surface area was studied on the same instrument, performing H₂ temperature programmed desorption (H₂-TPD) following H₂ chemisorption. A mass of approximately 100 mg of catalyst was reduced under a 10% H₂/Ar mixture, heating them up to 400 °C at 2.0 °C min⁻¹ and keeping this temperature for 1.0 h. The sample was then purged with Ar for 1.0 h. The temperature was then reduced to 50 °C under Ar and pulses of a 10% H₂/Ar mixture were sent on the catalyst until the saturation was reached (similar consecutive H₂ peaks measured by TCD). The system was then purged under Ar for 30 min and then heated up to 900 °C with a ramp of 15 °C min⁻¹ to desorb hydrogen from the surface. The amount of hydrogen desorbed was followed by TCD and quantitatively determined.

2.3. Catalytic tests

Catalytic tests were performed in a continuous tubular quartz reactor (length: 30 cm; internal diameter: 3.0 cm) located in a programmable furnace. The catalytic bed temperature was controlled by a thermocouple placed in the middle of the catalytic bed. The gases were fed to the reactor from gas tanks using mass flow controllers, while water was fed by a micro-pump and fully vaporized. The outlet gas passed through a cold trap to condense the steam. The dry gas was then analysed online by a micro-GC (Hewlett Packard, Quad Series Micro GC) equipped with TCD detectors and two columns: Molar sieve 5 Å (MS5A) was used to separate H₂, N₂, CH₄ et CO; PoraPlot U (PPU) was used to separate CH₄, CO₂ and traces of C₂H₆. Nitrogen was also fed and used as an internal standard.

The catalyst was activated before the catalytic tests by reduction in a H₂/N₂ mixture (36/5 mL.min⁻¹). The temperature was raised to 400 °C at 2.0 °C min⁻¹ and kept for 6 h at this temperature. After reduction, the catalysts were tested in CO/CO₂ co-methanation with a 4% H₂ excess considering CO_x methanation. The tests were conducted at atmospheric pressure and a GHSV of 45,000 h⁻¹ (STP). In the case of post co-electrolysis

1
2
3 1 conditions, methane and steam were added to the gas flow, after catalyst stabilization under co-methanation
4 2 conditions. Consequently, GHSV increased to 50,000 h⁻¹ (STP) at this stage. Table 1 reports molar composition
5 3 and employed flows for co-methanation and post co-electrolysis. Reactivity tests were conducted for 1.0 h
6 4 at successively 250, 300, 350, 400 and 450 °C.

8 5 The results were expressed in terms of methane yield which was calculated as expressed in equation 4.

11 6
$$CH_4 \text{ yield} = \frac{F_{CH_4}^{out} - F_{CH_4}^{in}}{F_{CO_2}^{in}} \text{Eq. 4}$$

13 7 where F_i refers to the molar flow of compound i.

15 8 *Table 1: molar composition and gas fluxes for the co-methanation and post co-electrolysis conditions.*

		H ₂	CO	CO ₂	CH ₄	H ₂ O	GHSV (h ⁻¹ , STP)
Co-methanation	Molar composition (%)	78	13	9.0	/	/	45,000
	Flow (NmL.min ⁻¹)	31.5	5.4	3.6	/	/	
Post co-electrolysis	Molar composition (%)	70	12	8.0	5.0	5.0	50,000
	Flow (NmL.min ⁻¹)	31.5	5.4	3.6	2.3	2.3	

30 10 **3. Results and discussion**

32 11 **3.1. Catalyst characterization**

33 12 The adsorption isotherms of the three supports are reported in Figure 1. CZP-CP and CZP-SG are characterized
34 13 by type IV isotherms with an H2 hysteresis [36] indicating a mesoporous structure with ink-bottled like pores,
35 14 which may be formed from interparticle porosity. Sol-gel and coprecipitation syntheses produce materials
36 15 composed of particles with low internal porosity, though pores are formed by the stacking of the different
37 16 particles. The isotherm of CZP-CC is also of type IV, but presents an H1 hysteresis, found at high P/P₀ values.
38 17 This is characteristic of mesoporous materials with cylindrical pores of uniform size. After Ni impregnation
39 18 the structures maintain the same morphologies, though the total adsorbed volume slightly decreases,
40 19 indicating a decrease in total surface area and pore volume. BJH model allowed to determine the pore
41 20 characteristics (Figure 2). All samples display a uniform pore size, centered at 3 and 5 nm for CZP-SG and CZP-
42 21 CP, while larger pores around 13 nm characterize CZP-CC. In general, CZP-CC displays a much higher BET
43 22 surface area (125 m² g⁻¹) than CZP-CP (69 m² g⁻¹) and CZP-SG (54 m² g⁻¹). The templating effect of SiO₂ in the
44 23 colloidal combustion synthesis allowed the formation of a particular pore structure with cylindrical pores,
45 24 which is responsible for the high surface area of this sample [28]. In contrast, a less porous matrix
46 25 characterizes CZP-CP and CZP-SG, where an interparticle porosity is encountered. The higher porosity of CZP-
47 26 CC contributes to reducing its apparent density, which is three to four times lower than that of other samples.

51 28 The trend in surface and pore morphology is also maintained after impregnation with Ni, followed by
52 29 calcination at 500 °C. These processes provide a slight decrease in these characteristics (Table 2) due to
53 30 sintering of support during calcination and the partial blocking of the pores by Ni.

* corresponding author : annececile.roger@unistra.fr

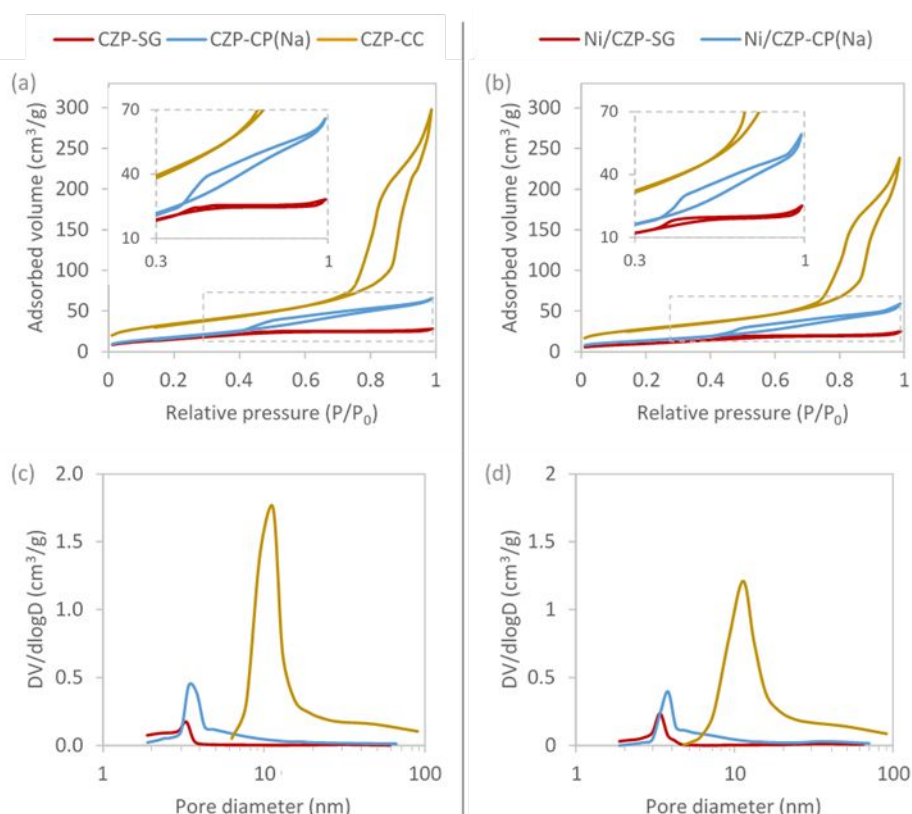


Figure 2: Isothermal plots of: (a) CZP-SG (red), CZP-CP (blue) and CZP-CC (orange) and (b) (Ni/CZP-SG (red), Ni/CZP-CP (blue) and Ni/CZP-CC (orange); and pore size distribution of: (c) CZP-SG (red), CZP-CP (blue) and CZP-CC (orange) and (d) (Ni/CZP-SG (red), Ni/CZP-CP (blue) and Ni/CZP-CC (orange)

Table 2: Surface area pore volume and average pore diameter for bare supports (CZP-SG, CZP-CP, CZP-CC and CZ-CP) and impregnated catalysts (Ni/CZP-SG, Ni/CZP-CP, Ni/CZP-CC and Ni/CZ-CP).

	CZP-SG	Ni/CZP-SG	CZP-CP	Ni/CZP-CP	CZP-CC	Ni/CZP-CC	CZ-CP	Ni/CZ-CP
S_{BET} ($\text{m}^2 \text{g}^{-1}$)	54	32	69	52	125	112	51	38
V_{pores} ($\text{cm}^3 \text{g}^{-1}$)	0.04	0.04	0.11	0.10	0.48	0.41	0.90	0.70
D_{pores} (nm)	3	4	5	6	13	14	5	5

The morphology of the CZP-CP catalyst was compared to that of the CZ-CP catalyst (Figure 3 and Table 2), to assess how the presence of Pr affects the morphological characteristics of the sample. A slightly lower surface area was observed for CZ-CP, both as bare support and after Ni impregnation (Table 2). Both isotherms and pore distribution (Figure 3) are similar and show a Type IV isotherm, an H2 isotherm and a narrow pore size centered at 5 nm. This indicates the presence of a mesoporous material, as previously described for CZP-CP. In general, the presence of Pr did not appear to affect the pore shape and size to any great extent, although it did provide a slight increase in surface area.

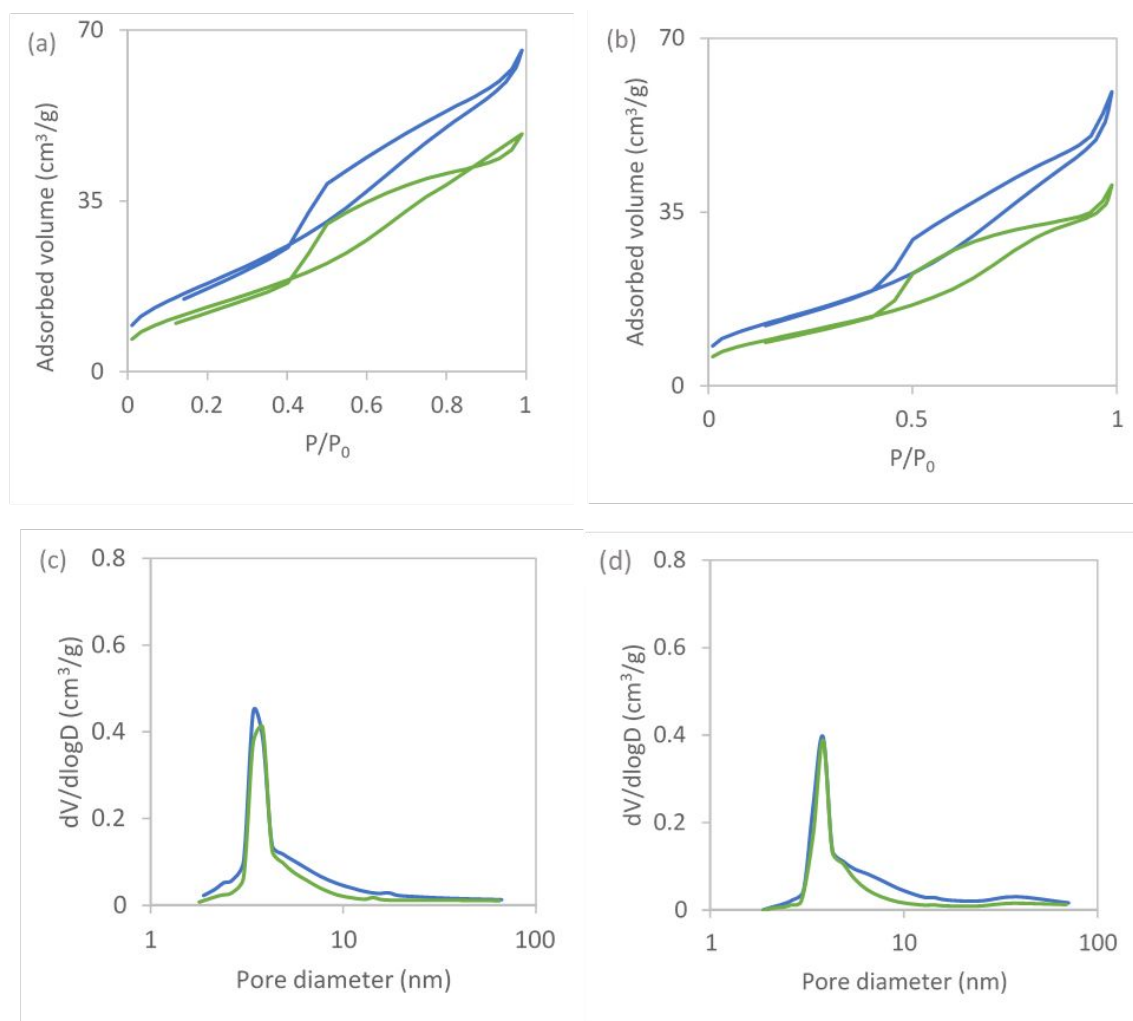


Figure 3: Isothermal plots: (a) CZP-CP (blue) and CZ-CP (green) and (b) Ni/CZP-CP (blue) and Ni/CZ-CP (green); and pore size distribution of (c) CZP-CP (blue) and CZ-CP (green) and (d) Ni/CZP-CP (blue) and Ni/CZ-CP (green).

The results of the XRD analyses of both bare and impregnated supports before reduction are reported in Figure 4 and Table 3. The sol-gel and colloidal combustion syntheses allowed to obtain mixed oxide structures shown by the presence of four broad reflections, ascribable to a tetragonal phase. These phases have a pseudo-cubic cell parameter (called a) of 5.24 and 5.23 Å, respectively. This phase is typical of ceria-zirconia solid solutions, in which both cations are dispersed in the same tetragonal structure. As no praseodymium oxide phase was detected, it can be assumed that Pr was also integrated into the mixed oxide structures, although its crystallization as single oxide cannot be excluded due to its low content and/or possible small crystallites. Two different phases were obtained by the coprecipitation synthesis. For the sol-gel support, the reflections are “split” toward lower and higher diffraction angles with respect to the nominal $\text{Ce}_{0.33}\text{Zr}_{0.63}\text{Pr}_{0.04}\text{O}_{1.99}$ phase. These two phases are indicative of a CeO_2 cubic phase (lower angles, larger cell) and a Zr-enriched tetragonal phase (higher angles, smaller cell). The pseudo-cubic lattice parameter a of the CeO_2 phase (on the 220 plan reflection at 48.0°) was calculated to be 5.41 Å, which is equal to the value reported for pure CeO_2 , while a pseudo-cubic lattice parameter of 5.19 Å were obtained for the second mixed oxide phase. This value is smaller than that obtained by the other synthetic methods, due to the lower content of Ce^{4+} which possesses a higher ionic radius than Zr^{4+} in eight-fold coordination. Again, Pr may be incorporated in both phases or crystallized as single oxide, in both cases below the detection threshold. However, it is difficult to assess this from the lattice parameter a due to the similar ionic radius of Ce^{4+} and Pr^{4+} (0.97 and 0.96 Å). The same phases are also found after Ni impregnation, together with a NiO phase. Scherrer equation allowed to calculate the NiO crystallite average size, which resulted to follow the order:

Ni/CZP-SG (25 nm) > Ni/CZP-CP (20 nm) >> Ni/CZP-CC (11 nm). This is in line with BET surface areas of the bare supports which follow the order: CZP-SG ($54 \text{ m}^2 \text{ g}^{-1}$) < Ni/CZP-CP ($69 \text{ m}^2 \text{ g}^{-1}$) << Ni/CZP-CC ($125 \text{ m}^2 \text{ g}^{-1}$). As expected, higher surface areas of the support allowed for better dispersion of NiO on the surface.

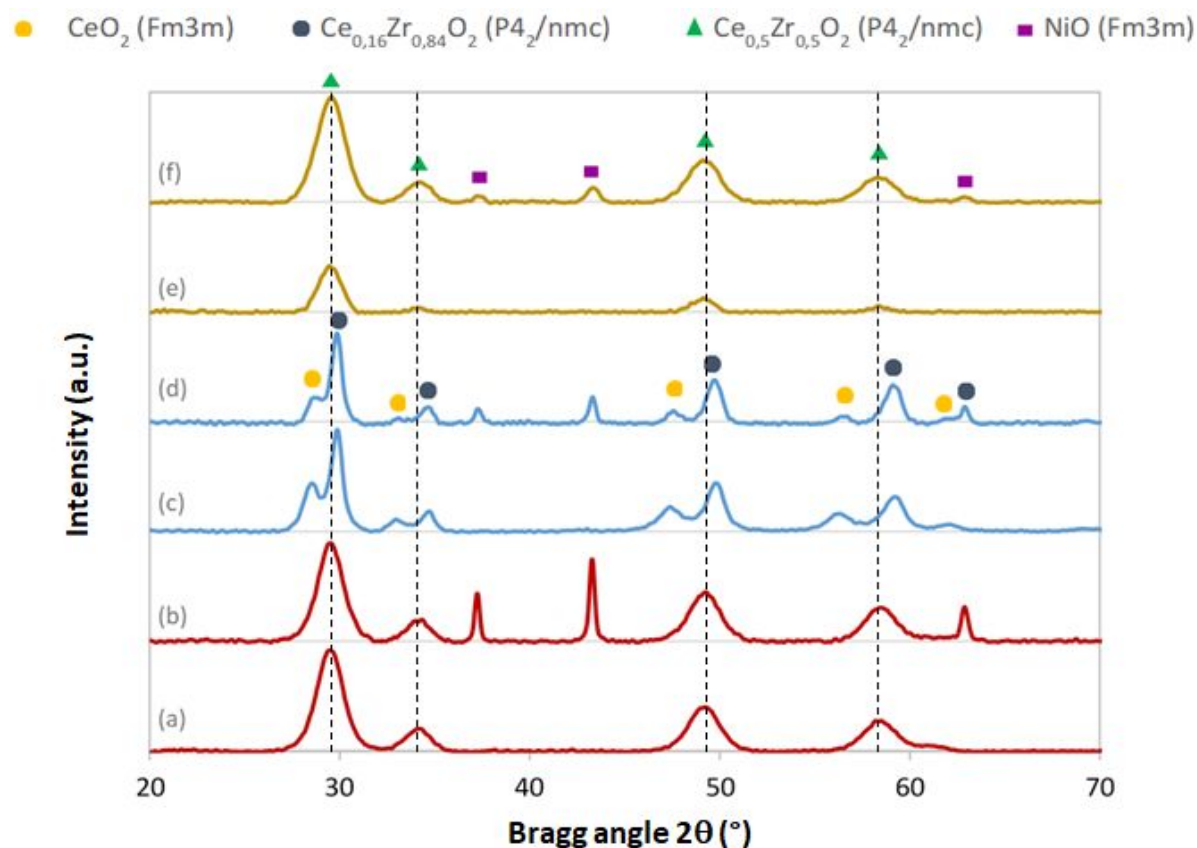


Figure 4: X-ray diffractograms of the bare supports and impregnated catalysts: (a) CZP-SG, (b) Ni/CZP-SG (c) CZP-CP, (d) Ni/CZP-CP, (e) CZP-CC and (f) Ni/CZP-CC. Dotted lines correspond to the position of main diffraction peaks of $\text{Ce}_{0.5}\text{Zr}_{0.5}\text{O}_2$ $P4_2/nmc$ crystalline structure.

Table 3: Pseudo-cubic lattice parameter a and average crystallite dimension of the different phases detected by XRD on impregnated catalysts (Ni/CZP-SG, Ni/CZP-CP, Ni/CZP-CC and Ni/CZ-CP).

		Ni/CZP-SG	Ni/CZP-CP	Ni/CZP-CC	Ni/CZ-CP
Catalysts	a_{CeO_2} (Å)	-	5.41	-	5.40
	D_{CeO_2} (nm)	-	8	-	9
	$a_{\text{CeO}_2\text{-ZrO}_2}$ (Å)	5.24	5.20	5.23	5.18
	$D_{\text{CeO}_2\text{-ZrO}_2}$ (nm)	5	8	5	9
	a_{NiO} (Å)	4.18	4.18	4.17	4.18
	D_{NiO} (nm)	25	20	11	21

Figure 5 shows the diffractograms of the Ni/CZ-CP and Ni/CZP-CP catalysts. As already discussed above for Ni/CZP-CP, the analysis of Ni/CZ-CP catalyst indicates the presence of pure CeO_2 as well as a mixed oxide enriched in Zr. By analysing the cell parameter reported in Table 3, it can be noted that Ni/CZP possesses a slightly higher value of a (5.20 Å vs 5.18 Å) for the mixed oxide compared to Ni/CZ. This is probably due to the presence of Pr^{3+} which has a larger ionic radius than Zr, in this phase. The lattice parameter of the ceria

1
2
3
4
5
6
7
8
9
10
11
12
13
14
15
16
17
18
19
20
21
22
23
24
25
26
27
28
29
30
31
32
33
34
35
36
37
38
39
40
41
42
43
44
45
46
47
48
49
50
51
52
53
54
55
56
57
58
59
60

phase of Ni/CZP is also slightly higher than that of the ceria phase in Ni/CP (5.41 Å vs 5.20 Å). As the lattice parameters of both phases are slightly higher for the Pr-containing sample (Table 3), it can be assumed that this element is present in the structure of both phases: ceria and Zr-enriched mixed oxide. The dimensions of the NiO crystallites are similar for both samples, possibly related to the similar surface areas of the two supports, which influence the distribution of NiO.

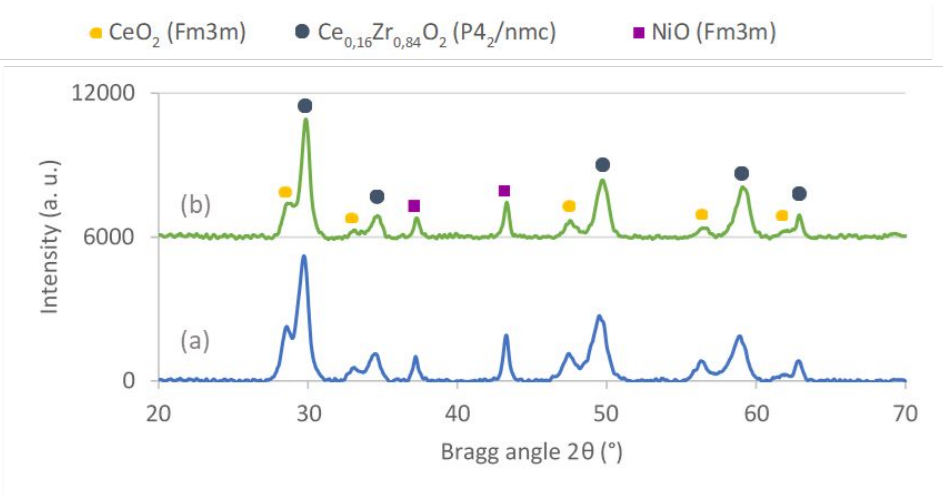


Figure 5: X-ray diffractograms of the impregnated catalysts: (a) Ni/CZP-CP and (b) Ni/CZ-CP.

The morphology and composition of the support were studied by SEM-EDX analysis (Figure 6). A relatively flat surface is obtained with the pseudo sol-gel synthesis, which explains the low porosity and low surface area observed by nitrogen physisorption analysis. The coprecipitation synthesis provides a rougher surface than the sol-gel method, while spherical pores can be observed on CZP-CC. This is in agreement with the morphology detected by nitrogen physisorption and is caused by the dissolution of SiO₂ spheres by NaOH.

* corresponding author : annececile.roger@unistra.fr

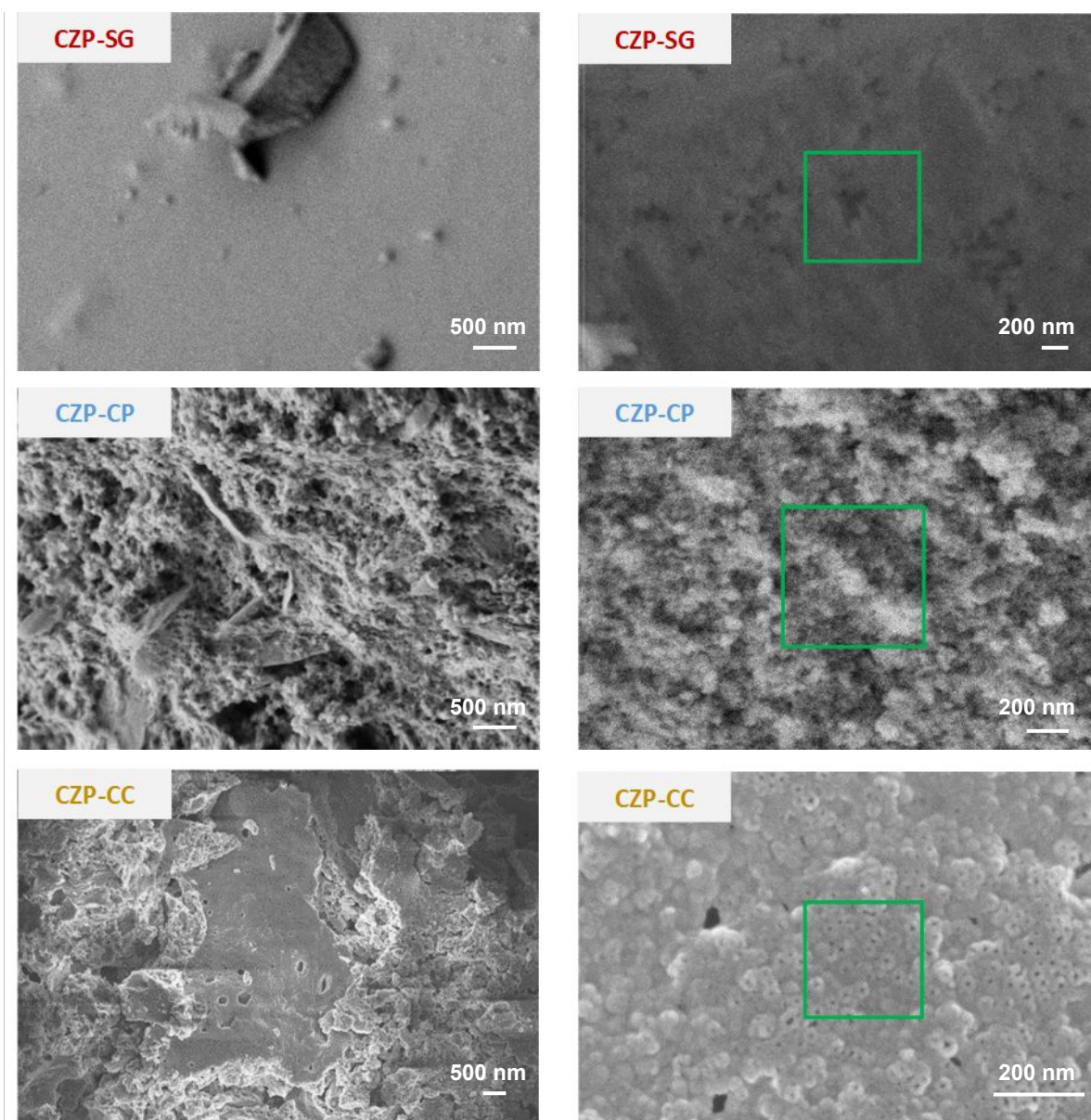


Figure 6: SEM analysis carried out on CZP-SG, CZP-CP and CZP-CC at different magnification; the marked areas (green squares) were analysed by EDX.

The composition of the samples (wt%) determined by EDX (Table 4), revealed similar values to those expected, calculated on the precursors amount (CeO_2 40wt%, ZrO_2 55wt%, Pr_6O_{11} 5wt%). The presence of sodium was found, together with Si, on the sample prepared by colloidal combustion. Nevertheless, half of SiO_2 has been removed by NaOH treatment, as shown by EDX of CZP-CC sample before SiO_2 dissolution.

Table 4: Samples composition (wt%) determined by EDX analysis on the areas of CZP-SG, CZP-CP and CZP-CC marked in Figure 6.

wt%	Theoretic	CZP -SG	CZP-CP	CZP-CC- SiO_2 precursor	CZP-CC
-----	-----------	---------	--------	-------------------------------------	--------

* corresponding author : annececile.roger@unistra.fr

CeO₂	40.0	39.7	39.3	31.4	37.1
ZrO₂	55.0	56.5	54.8	33.8	41.9
Pr₆O₁₁	5.0	3.8	5.9	5.3	6.3
Na₂O	-	-	-	-	2.6
SiO₂	-	-	-	29.5	12.1

The reducibility of the synthesized supports and catalysts was analysed by temperature programmed reduction (TPR) (Figure 7 and Table 5). One broad peak with maxima around 570-600 °C characterizes the reduction profile of bare CZP-SG and CZP-CC. From the literature, it is well known that pure CeO₂ presents two reduction peaks related to the reduction of surface ceria (530°C) and bulk ceria (820°C), respectively, into Ce₂O₃ [35,37]. The addition of Zr [38] and Pr [14,21] increases the oxygen mobility of the oxide, resulting in a more homogeneous reduction of both surface and bulk ceria are reduced simultaneously, reducing the reduction temperature of bulk ceria [38]. The reduction peak of CZP-CP is broader, with a wide shoulder around 400 °C. This is due to the presence of two phases, as detected by XRD. The addition of Ni on the supports allows decreasing the reduction temperature of Ce thanks to the spillover effect provided by the presence of metal, where hydrogen is dissociatively adsorbed and then transferred to the support. The spillover effect is logically less important for Ni/CZP-CC due to the presence of silica which may act as a barrier for the migration of hydrogen to ceria. The TPR profiles of Ni/CZP-CP and Ni/CZP-SG are similar, they show the main peak at around 380-400 °C, characteristic of bulk NiO, in addition to a broad consumption of hydrogen between 250 and 600 °C due to the reduction of surface and bulk ceria. Table 5 reports hydrogen consumption during TPR and percentage of reduced Ce, calculated assuming a total NiO reduction. The bare supports did not show a total Ce reduction with similar reducibility of around 80%. In all cases Ni impregnation increases reducibility by hydrogen spillover and allows the reduction of the whole CeO₂ to Ce₂O₃.

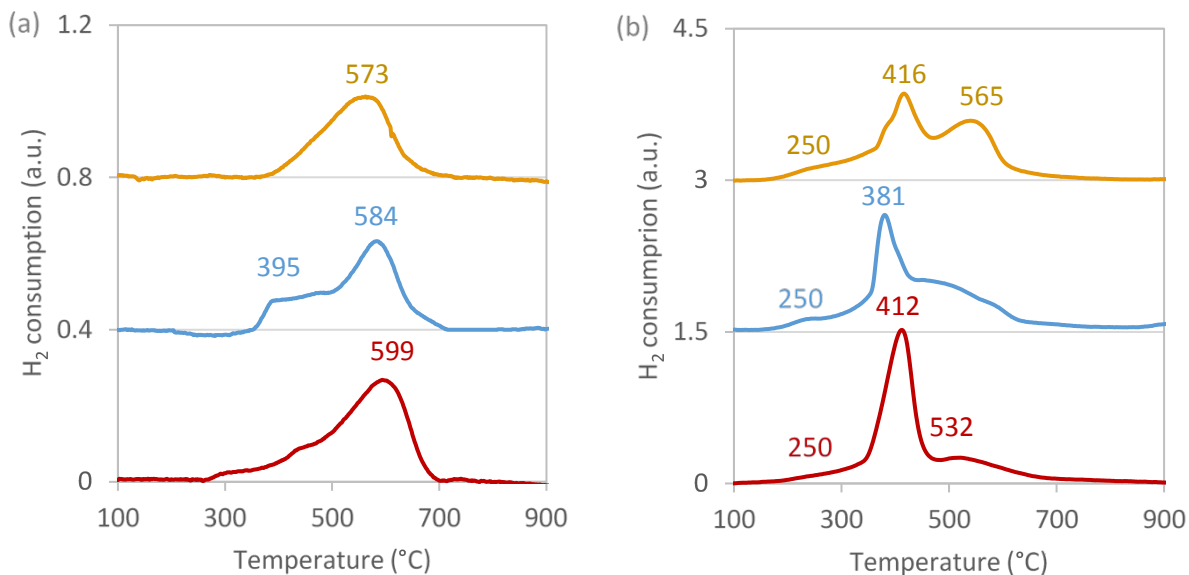


Figure 7: Temperature programmed reduction of: (a) CZP-SG (red), CZP-CP (blue) and CZP-CC (orange) and (b) the impregnated catalysts Ni/CZP-SG (red), Ni/CZP-CP (blue) and Ni/CZP-CC (orange).

* corresponding author : annececile.roger@unistra.fr

Table 5: Hydrogen consumption and calculated Ce reduction of the bare supports (CZP-SG, CZP-CP and CZP-CC) and impregnated catalysts (Ni/CZP-SG, Ni/CZP-CP and Ni/CZP-CC).

	CZP-SG	Ni/CZP-SG	CZP-CP	Ni/CZP-CP	CZP-CC	Ni/CZP-CC	CZ-CP	Ni/CZ-CP
H₂ consumption (mmol/g)	1.04	2.89	1.04	2.85	1.06	2.85	1.12	2.90
Ce⁴⁺ reduction (%)	79	100	79	98	80	98	92	100

A comparison between the TPR analysis of the coprecipitated samples with and without Pr is presented in Figure 8 and Table 5. Similar patterns were recorded for both samples, although a higher Ce⁴⁺ reduction was achieved with CZ-CP sample. Total Ce⁴⁺ reduction occurs after impregnation with NiO for both samples, thanks to the hydrogen spillover effect provided by Ni. However, the reduction peak of Ni/CZP-CP is found at a higher temperature, which may be due to a stronger interaction between Ni and the support that reduced reducibility.

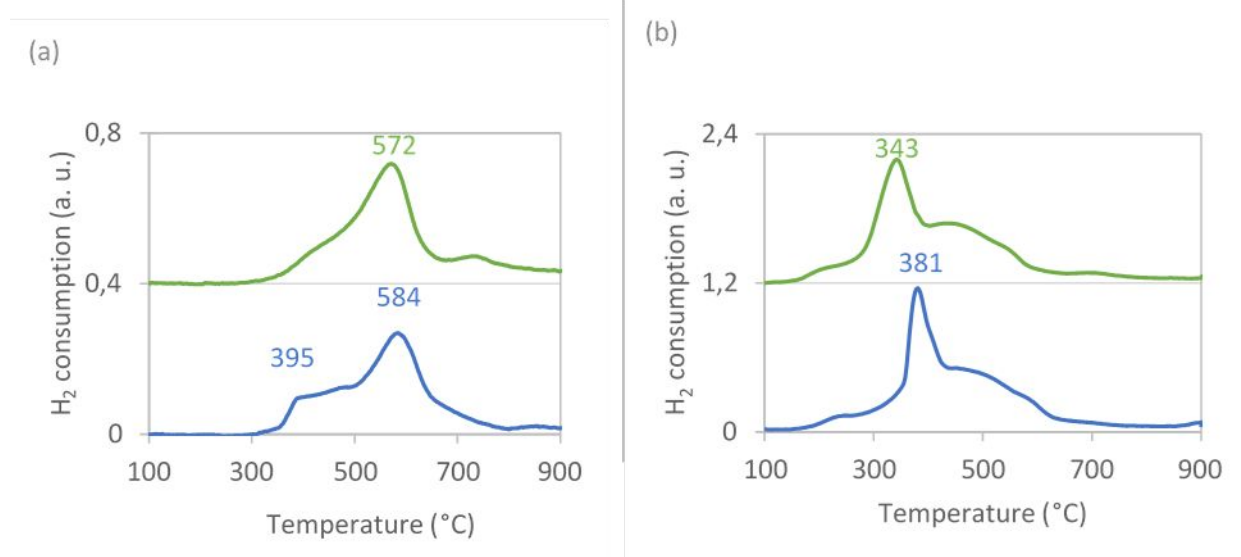


Figure 8: Temperature programmed reduction of: (a) CZ-CP (green) and CZP-CP (blue) and (b) the impregnated catalysts Ni/CZ-CP (green) and Ni/CZP-CP (blue).

Ni surface area was estimated by H₂ temperature programmed desorption (H₂-TPD) (Figure 9). The sol-gel catalyst displays a broad peak at high temperatures, centered around 530 °C and a smaller one at 140 °C. The coprecipitated and colloidal combustion catalyst exhibit a peak at low temperature (<135 °C) one around 300 °C and one over 500 °C. Integration of these peaks allowed to calculate Ni surface considering an average surface area occupied by a Ni atom in a face-centered cubic structure for an equivalent exposure of the (111), (100) and (110) planes of $6.51 \cdot 10^{-20} \text{ m}^2$ [39], area. It is then possible to determine Ni dispersion and particle dimension, hypothesising a H/Ni_{surf} ratio of 1.0 and the presence of semi-spherical Ni particles, not inserted inside the support structure (Table 6). The higher support surface area obtained by colloidal combustion allowed for a better Ni dispersion, reducing the particle dimension, increasing Ni dispersion. The trend of particle size dimension is similar to that of NiO average crystallite size dimension calculated by XRD analysis, suggesting that the particle dimension is defined during the impregnation step.

* corresponding author : annececile.roger@unistra.fr

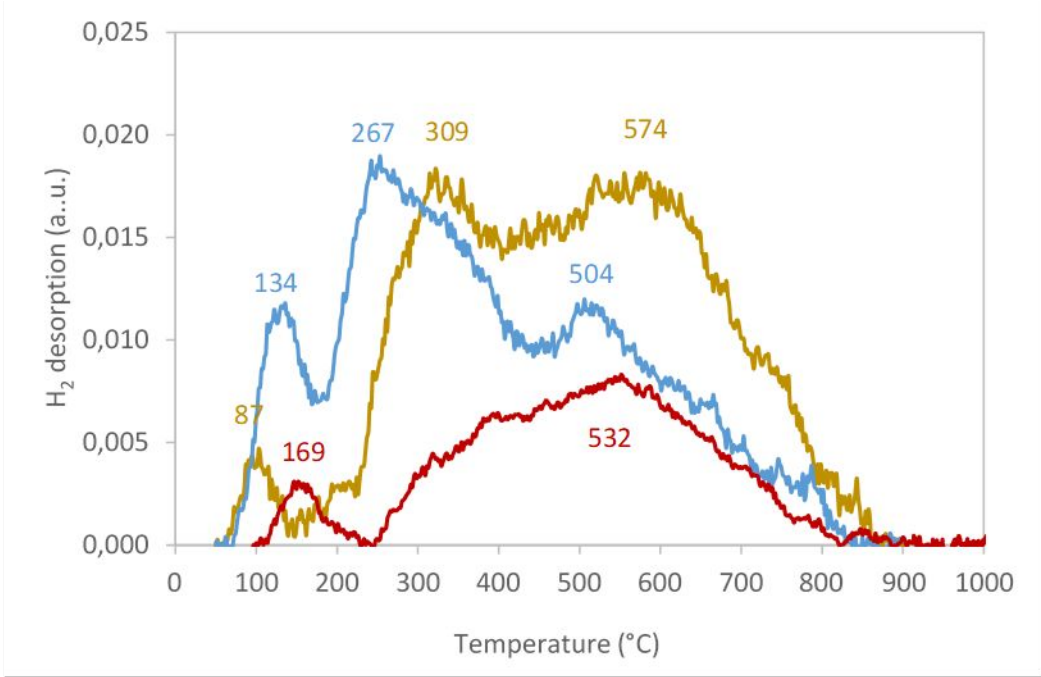


Figure 9: H₂ temperature programmed desorption of Ni/CZP-SG (red), Ni/CZP-CP (blue) and Ni/CZP-CC (orange).

Table 6: Desorbed hydrogen and calculated Ni surface area, Ni dispersion and particle dimension for Ni/CZP-SG, Ni/CZP-CP and Ni/CZP-CC.

	Ni/CZP-SG	Ni/CZP-CP	Ni/CZP-CC	Ni/CZ-CP
Desorbed H ₂ (mmol/g _{cat})	0.052	0.087	0.106	0.057
S _{Ni} ^a (m ² /g)	4.0	6.8	8.3	4.4
Dispersion NP (%)	6	10	12	7
D _{Ni} ^a (nm)	17	10	8	15

Compared to the Pr-containing sample, the H₂-TPD of Ni/CZ-CP showed the presence of a small peak at low temperature followed by a broader one (Figure 10). Less hydrogen was desorbed from Ni/CZ-CP, indicating a lower surface area of Ni, consistent with bigger particles. The dispersion of Ni is probably favoured by the presence of Pr and the consistent stronger metal-support interaction which increased the reduction temperature but favoured the formation of small particles, better inserted in the support.

* corresponding author : annececile.roger@unistra.fr

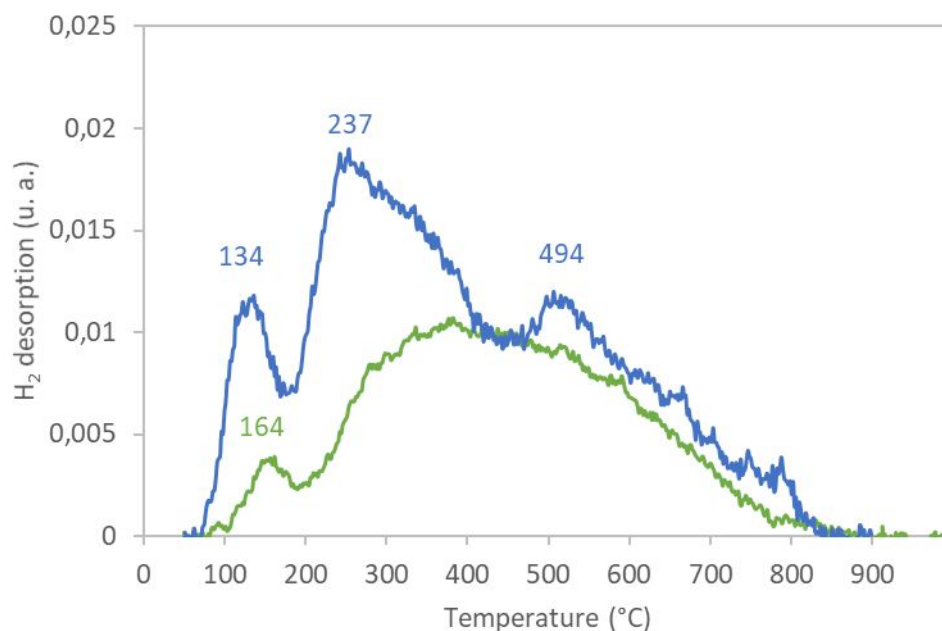


Figure 10: H_2 temperature programmed desorption of Ni/CZ-CP (green) and Ni/CZP-CP (blue).

3.2. Catalytic tests

Two reaction conditions were studied on the synthesized catalysts, namely CO/CO_2 co-methanation and post co-electrolysis mixture. Figure 11 shows the results of the catalytic tests in terms of methane yield. In all cases, the methane selectivity was above 99% with only traces of ethane as another carbon-containing product. At 250 °C, no activity was observed under either condition. However, Ni/CZP-CP showed a high methane yield of 79 % already at 270 °C. This catalyst outperforms the other two at higher temperatures, giving a methane yield of 87%. The catalytic methanation yield of the samples at low temperatures is consistent with the availability of hydrogen in this temperature range, as can be seen in the H_2 -TPD profiles (Figure 8). By increasing the temperature to 400 °C and above, the sol-gel catalyst achieved the performances of Ni/CZP-CC, whose yield increases slightly in the same range. Nevertheless, the highest activity was provided by Ni/CZP-CP, which gave higher yields than the other ones in a wide temperature range and was able to reach the thermodynamic equilibrium at 450 °C. The highest yield was obtained at 300 °C (87%), while it slightly decreased at higher temperatures due to the less favourable thermodynamic conditions.

When submitted to post co-electrolysis conditions (Figure 11 b), where also CH_4 and H_2O were present, all catalysts reduced their activity, especially at 300 °C, compared to the co-methanation mixture. Ni/CZP-SG was the most affected and reached the performances of Ni/CZP-CC only at 450 °C, at thermodynamic equilibrium. Smaller drops were displayed by the other two catalysts. These materials provided high conversions, also under these more discriminating conditions. Ni/CZP-CP gave the highest yield of 85% at 300 °C and values close to the thermodynamic equilibrium at higher temperatures.

In a complete kinetic study of methanation on Ni/alumina catalyst, Champon *et al.* [40] studied the effect of methane and water on the rate of methane formation under conditions close to those of the present study. While methane was shown to have no significant impact in the range of temperature studied, the presence of water negatively impacted methane formation. Inhibition by water was modeled by competitive adsorption on active sites. The model fits well the CH_4 formation rate data of CO_2 methanation. In our case, the strong impact on methane yield under post-coelectrolysis conditions is thus thought to be solely due to water in the stream. Competitive adsorption has a more negative impact on catalysts with a low number of active sites, which explains the much lower performance of the Ni/CZP-SG catalyst in the presence of water.

1
2
3
4
5
6
7
8
9
10
11
12
13
14
15
16
17
18
19
20
21
22
23
24
25
26
27
28
29
30
31
32
33
34
35
36
37
38
39
40
41
42
43
44
45
46
47
48
49
50
51
52
53
54
55
56
57
58
59
60

The sample prepared by pseudo sol-gel was characterized by the lowest Ni surface area (Table 6), which may explain its low methanation activity and the fact that it is strongly affected by the presence of water in post-co-electrolysis conditions. However, the catalytic activity is not directly related to the value of the metallic surface. It has been reported that the methanation reaction occurs mainly at the interface between Ni and the Ce-based support [29,41–43]. Thus, the presence of SiO₂ in the colloidal combustion sample Ni/CZP-CC, as discussed from the TPR profile, disfavors the Ni/support interfaces, which is detrimental to the catalytic activity, despite the higher metallic surface area. This is consistent with the work of Yang *et al.* [44] on mesoporous ceria for CO oxidation. Ni/CZP-CP high activity was due to a combination of properties that are reported to affect methanation activity, i.e., Ni surface area [45], support surface area, mesoporosity [25] and metal/ceria-based support interaction [30]. These properties contributed to make the coprecipitated catalyst the most active in both co-methanation and post electrolysis conditions.

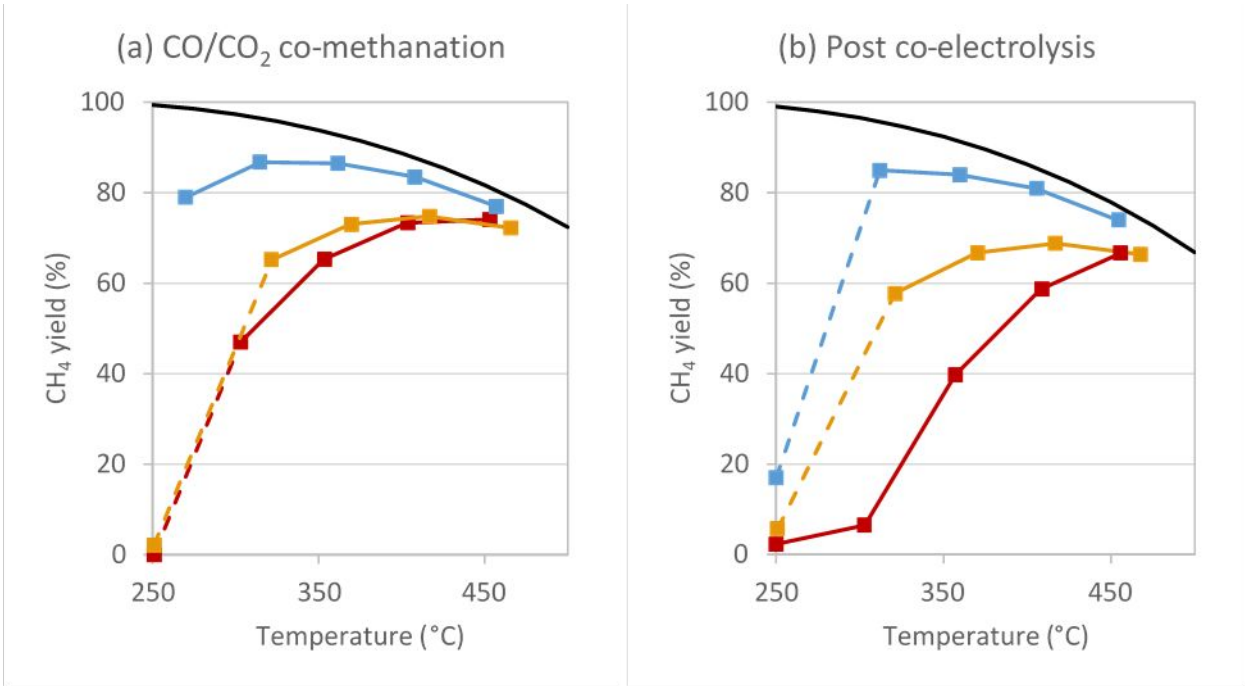


Figure 11: Experimental equilibrium methane yield obtained at different temperatures for (a) CO/CO₂ co-methanation conditions (P_{atm} , 45000 h⁻¹, H₂/CO_x = 3.54 and CO/CO₂ = 1.44) and for (b) post co-electrolysis conditions (P_{atm} , 50,000 h⁻¹, molar ratios: H₂/CO_x = 3.50 and CO/CO₂ = 1.50, H₂/CH₄ = 14.0, H₂/H₂O = 14.0) over Ni/CZP-SG (red), Ni/CZP-CP (blue) and Ni/CZP-CC (orange), thermodynamic equilibrium curves (black).

The effect of Pr presence in the coprecipitated samples on methanation activity is shown in Figure 12, where Ni/CZP-CP and Ni/CZ-CP are compared. A similar activity in CO/CO₂ co-methanation is reported by the two catalysts, which both showed a good methane yield even at low temperature (270 °C) and high GHSV. In post co-electrolysis conditions, similar results were also obtained at high temperatures, with methane yields that approach thermodynamic equilibrium. However, the Pr-containing sample provided higher activity below 300 °C with the highest yield of 85% recorded at this temperature. This is again in accordance with the H₂-TPD profiles of the samples.

The comparison with the literature on co-methanation is difficult. Co-methanation is generally dealing with the presence of CO in the CO₂ feed, far from the 60/40 molar CO/CO₂ ratio of the inlet flow of this work. By comparison with CO₂ methanation studies, among the catalysts of this study, those prepared by

* corresponding author : annececile.roger@unistra.fr

coprecipitation Ni/CZP-CP and Ni/CZ-CP compete with the best systems published in the literature. The production of methane at 300 °C is about 50-60 $\mu\text{molCH}_4 \text{ g}^{-1} \text{ s}^{-1}$ at GHSV of 45,000 h^{-1} for these catalysts, it places them in the most active systems among those studied in similar operating conditions for CO_2 methanation [46].

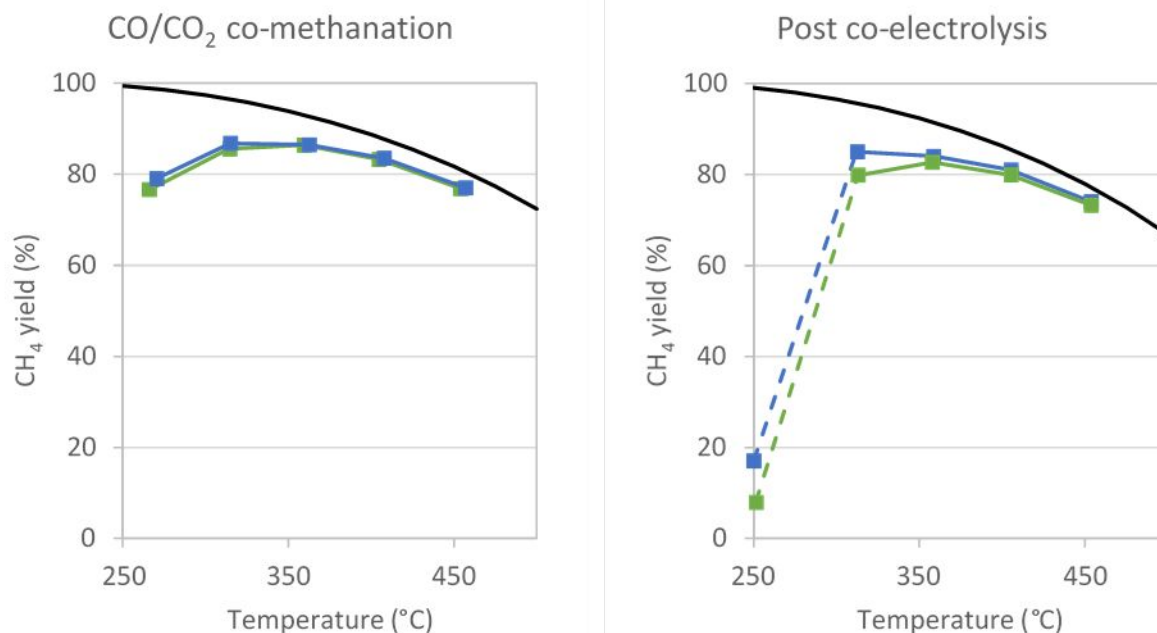


Figure 12: Experimental and equilibrium methane yield obtained at different temperatures at (a) CO/CO_2 co-methanation conditions (P_{atm} , 45,000 h^{-1} , $\text{H}_2/\text{CO}_x = 3.54$ and $\text{CO}/\text{CO}_2 = 1.44$) and post co-electrolysis conditions (P_{atm} , 50,000 h^{-1} , $\text{H}_2/\text{CO}_x = 3.50$ and $\text{CO}/\text{CO}_2 = 1.50$, $\text{H}_2/\text{CH}_4 = 14.00$, $\text{H}_2/\text{H}_2\text{O} = 14.00$) over Ni/CZ-CP (green) and Ni/CZP-CP (blue), thermodynamic values (black).

4. Conclusion

Three $\text{Ce}_{0.33}\text{Zr}_{0.63}\text{Pr}_{0.04}\text{O}_{1.99}$ catalytic supports were synthesized by three different techniques to investigate their effect on the support properties and catalytic performances. A pseudo sol-gel, coprecipitation and colloidal combustion were selected. Pseudo sol-gel and colloidal combustion provided the formation of a mixed oxide while segregated pure CeO_2 and a Ce-poor phase were obtained by coprecipitation. The presence of a SiO_2 templating agent allowed to obtain a high surface area, which provides a higher metallic dispersion after Ni impregnation, though SEM showed that part of Si was left on the sample, which decreases the H_2 -spillover from Ni to ceria. On the opposite, a higher metal support interaction was detected by TPR on the sol-gel and coprecipitated catalyst. When submitted to CO_2/CO co-methanation and a post co-electrolysis mixture the coprecipitated catalyst showed the best performances. This was linked with the combination of characteristics that contributed to enhancing the catalytic activity in the methanation reaction, i.e., high support metal interaction and reducibility, high surface area and mesoporosity, linked with good Ni dispersion and surface area. The effect of Pr showed to be favourable for the investigated reaction, giving higher methane yields at low temperatures.

5. Acknowledgments

* corresponding author : annececile.roger@unistra.fr

The authors thank the French ANR for funding the project CHOCHCO n° 13 SEED 0002 01.

6. References

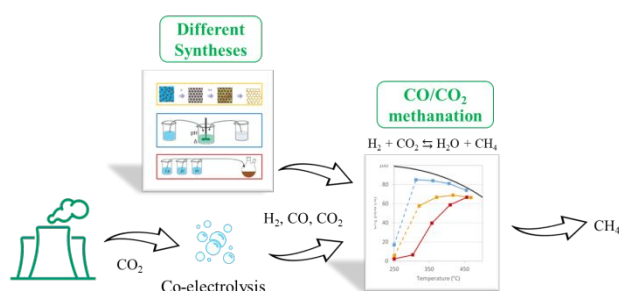
1. M. Child, D. Bogdanov, C. Breyer, The role of storage technologies for the transition to a 100% renewable energy system in Europe, *Energy Procedia*, 155 (2018), 44–60, <https://doi.org/10.1016/j.egypro.2018.11.067>.
2. A. Lewandowska-Bernat, U. Desideri, Opportunities of power-to-gas technology in different energy systems architectures, *Appl. Energ.*, 228 (2018) 57–67, <https://doi.org/10.1016/j.apenergy.2018.06.001>.
3. M. Bailera, P. Lisbona, L.M. Romeo, S. Espatolero, Power to Gas projects review: Lab, pilot and demo plants for storing renewable energy and CO₂, *Renew. Sust. Energ. Rev.*, 69 (2017) 292–312, <https://doi.org/10.1016/j.rser.2016.11.130>.
4. B. Lynch, A. Kiger, K. Hatipoglu, An overview of hydrogen electrical energy storage meeting energy demand with intermittent renewable resources, *Proceedings of the SoutheastCon 2016* pp. 1–6.
5. A. Demirbas, Future hydrogen economy and policy, *Energ. Source Part B*, 12 (2017) 172–181, <https://doi.org/10.1080/15567249.2014.950394>.
6. A. Martin, M.F. Agnoletti, E. Brangier, Users in the design of Hydrogen Energy Systems: A systematic review, *Int. J. Hydrogen Energ.*, 45 (2020) 11889–11900, <https://doi.org/10.1016/j.ijhydene.2020.02.163>.
7. D. Astiaso Garcia, Analysis of non-economic barriers for the deployment of hydrogen technologies and infrastructures in European countries, *Int. J. Hydrogen Energ.*, 42 (2017) 6435–6447, <https://doi.org/10.1016/j.ijhydene.2017.01.201>.
8. Q. Fu, C. Mabilat, M. Zahid, A. Brisse, L. Gautier, Syngas production via high-temperature steam/CO₂ co-electrolysis: an economic assessment, *Energ. Environ. Sci.*, 3 (2010) 1382–1397, <https://doi.org/10.1039/C0EE00092B>.
9. S.-W. Kim, H. Kim, K.J. Yoon, J.-H. Lee, B.-K. Kim, W. Choi, J.-H. Lee, J. Hong, Reactions and mass transport in high temperature co-electrolysis of steam/CO₂ mixtures for syngas production, *J. of Power Sources*, 280 (2015) 630–639, <https://doi.org/10.1016/j.jpowsour.2015.01.083>.
10. P. Frontera, A. Macario, M. Ferraro, P. Antonucci, Supported Catalysts for CO₂ Methanation: A Review, *Catalysts*, 7 (2017) 59–86, <https://doi.org/10.3390/catal7020059>.
11. J. Ashok, S. Pati, P. Hongmanorom, Z. Tianxi, C. Junmei, S.A. Kawi, A review of recent catalyst advances in CO₂ methanation processes, *Catal. Today*, 356 (2020) 471–489, <https://doi.org/10.1016/j.cattod.2020.07.023>.
12. J. Martínez, E. Hernández, S. Alfaro, R. López Medina, G. Valverde Aguilar, E. Albitier, M.A. Valenzuela, High Selectivity and Stability of Nickel Catalysts for CO₂ Methanation: Support Effects, *Catalysts*, 9 (2019) 24–36, <https://doi.org/10.3390/catal9010024>.
13. W. Gac, W. Zawadzki, M. Rotko, M. Greluk, G. Słowik, G. Kolb, Effects of support composition on the performance of nickel catalysts in CO₂ methanation reaction, *Catal. Today*, 357 (2020) 468–482, <https://doi.org/10.1016/j.cattod.2019.07.026>.
14. E. Aneggi, C. de Leitenburg, G. Dolcetti, A. Trovarelli, Promotional effect of rare earths and transition metals in the combustion of diesel soot over CeO₂ and CeO₂–ZrO₂, *Catal. Today*, 114 (2006) 40–47, <https://doi.org/10.1016/j.cattod.2006.02.008>.
15. T. Andana, M. Piumetti, S. Bensaid, N. Russo, D. Fino, R. Pirone, CO and Soot Oxidation over Ce-Zr-Pr Oxide Catalysts, *Nanoscale Res. Lett.*, 11 (2016) 278–286, <https://doi.org/10.1186/s11671-016-1494-6>.
16. F. Basile, R. Mafessanti, A. Fasolini, G. Fornasari, E. Lombardi, A. Vaccari, Effect of synthetic method on CeZr support and catalytic activity of related Rh catalyst in the oxidative reforming reaction, *J. Eur. Ceram. Soc.*, 39 (2019) 41–52, <https://doi.org/10.1016/j.jeurceramsoc.2018.01.047>.
17. A. Fasolini, S. Ruggieri, C. Femoni, F. Basile, Highly Active Catalysts Based on the Rh₄(CO)₁₂ Cluster Supported on Ce_{0.5}Zr_{0.5} and Zr Oxides for Low-Temperature Methane Steam Reforming, *Catalysts*, 9 (2019) 800–818, <https://doi.org/10.3390/catal9100800>.

* corresponding author : annececile.roger@unistra.fr

18. X. Yang, L. Yang, S. Lin, R. Zhou, New Insight into the Doping Effect of Pr_2O_3 on the Structure–Activity Relationship of $\text{Pd/CeO}_2\text{–ZrO}_2$ Catalysts by Raman and XRD Rietveld Analysis, *J. Phys. Chem. C*, 119 (2015) 6065–6074, <https://doi.org/10.1021/jp512606m>.
19. Z. Xiao, Y. Li, F. Hou, C. Wu, L. Pan, J. Zou, L. Wang, X. Zhang, G. Liu, G. Li, Engineering oxygen vacancies and nickel dispersion on CeO_2 by Pr doping for highly stable ethanol steam reforming, *Appl. Catal. B-Environ.*, 258 (2019) 117940–117968, <https://doi.org/10.1016/j.apcatb.2019.117940>.
20. V. Frizon, J.-M. Bassat, M. Pollet, E. Durand, J. Hernandez, K. Pajot, P. Vernoux, A. Demourgues, Tuning the Pr valence state to design high oxygen mobility, redox and transport properties in the $\text{CeO}_2\text{–ZrO}_2\text{–PrO}_x$ phase diagram, *J. Phys. Chem. C*, 123 (2019) 6351–6362, <https://doi.org/10.1021/acs.jpcc.8b11469>.
21. R. Si, Y.-W. Zhang, L.-M. Wang, S.-J. Li, B.-X. Lin, W.-S. Chu, Z.-Y. Wu, C.-H. Yan, Enhanced Thermal Stability and Oxygen Storage Capacity for $\text{Ce}_x\text{Zr}_{1-x}\text{O}_2$ ($x = 0.4\text{–}0.6$) Solid Solutions by Hydrothermally Homogenous Doping of Trivalent Rare Earths, *J. Phys. Chem. C*, 111 (2007) 787–794, <https://doi.org/10.1021/jp0630875>.
22. I. Iglesias, A. Quindimil, F. Mariño, U. De-La-Torre, J.R. González-Velasco, Zr promotion effect in CO_2 methanation over ceria supported nickel catalysts, *Int. J. Hydrogen Energ.*, 44 (2019) 1710–1719, <https://doi.org/10.1016/j.ijhydene.2018.11.059>.
23. F. Ocampo, B. Louis, A.C. Roger, Methanation of carbon dioxide over nickel-based $\text{Ce}_{0.72}\text{Zr}_{0.28}\text{O}_2$ mixed oxide catalysts prepared by sol–gel method, *Appl. Catal. A-Gen.*, 369 (2009) 90–96, <https://doi.org/10.1016/j.apcata.2009.09.005>.
24. F. Ocampo, B. Louis, L. Kiwi-Minsker, A.C. Roger, Effect of Ce/Zr composition and noble metal promotion on nickel based $\text{Ce}_x\text{Zr}_{1-x}\text{O}_2$ catalysts for carbon dioxide methanation, *Appl. Catal. A-Gen.*, 392 (2011) 36–44, <https://doi.org/10.1016/j.apcata.2010.10.025>.
25. M. Frey, G. Mignani, J. Jolly, A.-C. Roger, Effect of Physico-Chemical Properties of Ceria-Based Supports on the Carbon Dioxide Methanation Reaction, *Adv. Chem. Lett.*, 1 (2013) 257–263, <https://doi.org/10.1166/acl.2013.1039>.
26. G.I. Siakavelas, N.D. Charisiou, S. Alkhoori, A.A. Alkhoori, V. Sebastian, S.J. Hinder, M.A. Baker, I.V. Yentekakis, K. Polychronopoulou, M.A. Goula, Highly selective and stable nickel catalysts supported on ceria promoted with Sm_2O_3 , Pr_2O_3 and MgO for the CO_2 methanation, *Appl. Catal. B-Environ.*, 282 (2021) 119562–119564, <https://doi.org/10.1016/j.apcatb.2020.119562>.
27. S. Rossignol, F. Gérard, D. Duprez, Effect of the preparation method on the properties of zirconia ceria materials, *J. Mater. Chem.*, 9 (1999) 1615–1620, <https://doi.org/10.1039/A900536F>.
28. A.A. Voskanyan, K.-Y. Chan, C.-Y.V. Li, Colloidal Solution Combustion Synthesis: Toward Mass Production of a Crystalline Uniform Mesoporous CeO_2 Catalyst with Tunable Porosity, *Chem. Mater.*, 28 (2016) 2768–2775, <https://doi.org/10.1021/acs.chemmater.6b00505>.
29. P.A. Ussa Aldana, F. Ocampo, K. Kobl, B. Louis, F. Thibault-Starzyk, M. Daturi, P. Bazin, S. Thomas, A.C. Roger, Catalytic CO_2 valorization into CH_4 on Ni-based ceria-zirconia. Reaction mechanism by *operando* IR spectroscopy, *Catal. Today*, 215 (2013) 201–207, <https://doi.org/10.1016/j.cattod.2013.02.019>.
30. M. Li, H. Amari, A.C. van Veen, Metal-oxide interaction enhanced CO_2 activation in methanation over ceria supported nickel nanocrystallites, *Appl. Catal. B-Environ.*, 239 (2018) 27–35, <https://doi.org/10.1016/j.apcatb.2018.07.074>.
31. J. Sehested, S. Dahl, J. Jacobsen, J.R. Rostrup-Nielsen, Methanation of CO over Nickel: Mechanism and Kinetics at High H_2/CO Ratios, *J. Phys. Chem. B*, 109 (2005) 2432–2438, <https://doi.org/10.1021/jp040239s>.
32. M. Cai, J. Wen, W. Chu, X. Cheng, Z. Li, Methanation of carbon dioxide on $\text{Ni/ZrO}_2\text{–Al}_2\text{O}_3$ catalysts: Effects of ZrO_2 promoter and preparation method of novel $\text{ZrO}_2\text{–Al}_2\text{O}_3$ carrier, *J. Nat. Gas*, 20 (2011) 318–324, [https://doi.org/10.1016/S1003-9953\(10\)60187-9](https://doi.org/10.1016/S1003-9953(10)60187-9).
33. X. Yan, Y. Liu, B. Zhao, Z. Wang, Y. Wang, C. Liu, Methanation over Ni/SiO_2 : Effect of the catalyst preparation methodologies, *Int. J. Hydrogen Energ.*, 38 (2013) 2283–2291, <https://doi.org/10.1016/j.ijhydene.2012.12.024>.

34. Q. Liu, H. Yang, H. Dong, W. Zhang, B. Bian, Q. He, J. Yang, X. Meng, Z. Tian, G. Zhao, Effects of preparation method and Sm_2O_3 promoter on CO methanation by a mesoporous $\text{NiO-Sm}_2\text{O}_3/\text{Al}_2\text{O}_3$ catalyst, *New J. Chem.*, 42 (2018) 13096–13106, <https://doi.org/10.1039/C8NJ02282H>.
35. S. Letichevsky, C.A. Tellez, R.R. de Avillez, M.I.P. da Silva, M.A. Fraga, L.G. Appel, Obtaining $\text{CeO}_2\text{-ZrO}_2$ mixed oxides by coprecipitation: role of preparation conditions, *Appl. Catal. B-Environ.*, 58 (2005) 203–210, <https://doi.org/10.1016/j.apcatb.2004.10.014>.
36. R. Bacani, T.S. Martins, M.C.A. Fantini, D.G. Lamas, Structural studies of mesoporous $\text{ZrO}_2\text{-CeO}_2$ and $\text{ZrO}_2\text{-CeO}_2/\text{SiO}_2$ mixed oxides for catalytical applications, *J. Alloys Compd.*, 671 (2016) 396–402, <https://doi.org/10.1016/j.jallcom.2016.01.213>.
37. H. Zhu, Z. Qin, W. Shan, W. Shen, J. Wang, Pd/ $\text{CeO}_2\text{-TiO}_2$ catalyst for CO oxidation at low temperature: a TPR study with H_2 and CO as reducing agents, *J. Catal.*, 225 (2004) 267–277, <https://doi.org/10.1016/j.jcat.2004.04.006>.
38. C. de Leitenburg, A. Trovarelli, J. Llorca, F. Cavani, G. Bini, The effect of doping CeO_2 with zirconium in the oxidation of isobutene, *Appl. Catal. A-Gen.*, 139 (1996) 161–173, [https://doi.org/10.1016/0926-860X\(95\)00334-7](https://doi.org/10.1016/0926-860X(95)00334-7).
39. G. Bergeret, P. Gallezot, Particle Size and Dispersion Measurements, Chapter 3.1.2 Handbook of Heterogeneous Catalysis, second ed., G. Ertl, H. Knözinger, F. Schüth, J. Weitkamp Editors, Wiley, New York, 738–765 (2008).
40. I. Champon, A. Bengaouer, A. Chaise, S. Thomas, A.C. Roger, Carbon dioxide methanation kinetic model on a commercial $\text{Ni}/\text{Al}_2\text{O}_3$ catalyst, *J. CO₂ Utilization*, 34 (2019) 256–265, <https://doi.org/10.1016/j.jcou.2019.05.030>.
41. A. Cárdenas-Arenas, A. Quindimil, A. Davó-Quiñonero, E. Bailón-García, D. Lozano-Castelló, U. De-La-Torre, B. Pereda-Ayo, J.A. González-Marcos, J.R. González-Velasco, A. Bueno-López, Isotopic and in situ DRIFTS study of the CO_2 methanation mechanism using Ni/CeO_2 and $\text{Ni}/\text{Al}_2\text{O}_3$ catalysts, *Appl. Catal. B Environ.*, 265 (2020) 118538–118561, <https://doi.org/10.1016/j.apcatb.2019.118538>.
42. B. Miao, S.S. Khine Ma, X. Wang, H. Su, S. Hwa Chan, Catalysis mechanisms of CO_2 and CO methanation, *Catal. Sci. Technol.*, 6 (2016) 4048–4058, <https://doi.org/10.1039/C6CY00478D>.
43. F. Wang, S. He, H. Chen, B. Wang, L. Zheng, M. Wei, D.G. Evans, X. Duan, Active Site Dependent Reaction Mechanism over Ru/CeO_2 Catalyst toward CO_2 Methanation, *J. Am. Chem. Soc.*, 138 (2016) 6298–6305, <https://doi.org/10.1021/jacs.6b02762>.
44. P. Yang, S.Y. Zhou, J.H. Lei, Effect of templates on catalytic activity of ordered mesoporous ceria for CO oxidation, *Advanced Materials Research*, 95–98 (2014) 1033–1034, <https://doi.org/10.4028/www.scientific.net/AMR.1033-1034.95>
45. R. Razzaq, C. Li, N. Amin, S. Zhang, K. Suzuki, Co-methanation of Carbon Oxides over Nickel-Based $\text{Ce}_x\text{Zr}_{1-x}\text{O}_2$ Catalysts, *Energ. Fuels*, 27 (2013) 6955–6961, <https://doi.org/10.1021/ef401049v>.
46. G. Varvoutis, M. Lykaki, S. Stefa, V. Binas, G.E. Marnellos, M. Konsolakis, Deciphering the role of Ni particle size and nickel-ceria interfacial perimeter in the low-temperature CO_2 methanation reaction over remarkably active Ni/CeO_2 nanorods, *Appl. Catal. B-Environ.*, 297 (2021) 120401–120414, <https://doi.org/10.1016/j.apcatb.2021.120401>

TOC Graphic



* corresponding author : annececile.roger@unistra.fr